Engineered Science
DOI: https://dx.doi.org/10.30919/es2069

Modeling the Interaction of the Rolling Stock and the Track in the Emergency Braking Mode of a Passenger Train

Janat Musayev,[1] Algazy Zhauyt,[2,*] Vladimir Solonenko,[1] Kuanysh Alipbayev,[2] Nazgul Kaliyeva,[2] Gulbarshyn Smailova[3] and Nurgul Kurmangaliyeva[2]

Abstract

This paper investigates the interaction between rolling stock and railway track during the emergency braking of a passenger train. A detailed simulation model of a train consisting of a locomotive and twenty passenger cars was developed in the Universal Mechanism software environment. The model accounts for longitudinal, lateral, and vertical vibrations, as well as nonlinear elastic couplings and random track irregularities. Simulation results show that the estimated braking distance is 583 m, which complies with current regulatory standards. The analysis of coupler forces revealed that braking is generally shockless due to buffer devices, except at the locomotive-first car connection. Derailment is possible only under severe track irregularity conditions, while displacement of the rail-sleeper lattice caused by increased transverse forces does not result in derailment. The findings contribute to improving railway safety assessment and support the development of intelligent monitoring and warning systems for modern "smart train" applications.

Keywords: Railway dynamics; Emergency braking; Passenger train; Simulation modeling; Universal mechanism.
Received: 22 September 2025; Revised: 09 January 2026; Accepted: 28 January 2026
Article type: Research article.

1. Introduction

Emergency situations-such as the sudden appearance of pedestrians or animals on railway lines, loss of braking efficiency, or technical failures-require the train driver to apply an immediate braking command. Understanding the dynamic response of rolling stock and track during such emergency braking is critical for ensuring safety, preventing derailment, and optimizing braking performance. Earlier investigations by Musayev *et al.*,[1,2] Günay *et al.*,[3] and Zhu *et al.*[4] provided important foundations for studying braking dynamics, energy absorption, and structural design of braking systems. Other studies have examined wheel-rail contact forces,[5] track stiffness,[6–9] and rail irregularities,[10–11] highlighting that train-track interaction under dynamic loads remains a nonlinear, multi-parameter problem. Despite these advances, most prior works consider isolated vehicles or specific subsystems and rarely capture the coupled longitudinal, lateral, and vertical responses of an entire train during emergency braking.

Recent advancements in railway system modeling have benefited from virtual and co-simulation techniques,[12] data-driven signal processing for track defect detection,[13–16] and probabilistic reliability analyses of wheelsets and track components.[17,18] Additional progress in curving dynamics,[19–23] wheel-rail friction modeling,[24–30] and hunting stability assessment[31,32] has further improved the precision of multibody railway simulations. Despite these developments, most prior works focus on local subsystems or specific load cases rather than integrated full-train emergency braking.

Recent multibody dynamics approaches[33–41] have improved modeling of large train formations by accounting for nonlinear coupler-buffer behavior and brake propagation effects. Sharma[33] analyzed longitudinal-vibration coupling under braking; Cantone *et al.*[35] and Bosso *et al.*[36] evaluated in-train compressive forces and emergency braking distances; Krishna *et al.*[37] extended these models to overlong freight trains; and Burgelman *et al.*[38] proposed rapid derailment-risk evaluation methods. Zhao *et al.*[39] experimentally validated multibody simulations, and Zhai *et al.*[40] summarized theoretical advances in coupled train-track-bridge dynamics. However, most of these works focus on freight or short

[1]*Department of Rolling Stock, M. Tynyshpaev ALT University, Almaty, 050012, Kazakhstan*
[2]*Department of Aerospace and Electronic Engineering, Almaty University of Power Engineering and Telecommunications named after G. Daukeyev, Almaty, 050013, Kazakhstan*
[3]*Department of Mechanical Engineering, Satbayev University, Almaty, 050013, Kazakhstan*
[*]*Email:* a.zhauyt@aues.kz (A. Zhauyt)

trainsets and seldom represent passenger trains composed of multiple wagons. Moreover, the combined influence of random track irregularities, nonlinear elastic couplings, and braking-induced longitudinal forces remains insufficiently quantified, particularly for modern high-speed or intercity rolling stock.[41]

This study addresses these gaps by developing and validating a comprehensive multibody dynamic model of a full passenger train (one locomotive and twenty wagons) within the Universal Mechanism (UM) simulation environment.[34] The model integrates longitudinal, lateral, and vertical dynamics; wheel-rail contact and friction behavior; coupler and buffer devices; and braking torque generation. Simulations evaluate braking distance, longitudinal and frame forces, and derailment stability under realistic track irregularities. The research specifically solves the following problems:

1. constructing a full-train multibody model for emergency braking that includes nonlinear coupler-buffer interactions and track elasticity;
2. determining the critical roughness amplitudes and wavelengths leading to potential wheel derailment;
3. quantifying the effect of braking on longitudinal-force propagation and train stability.

The results improve understanding of coupled train–track dynamics during extreme deceleration and provide a validated framework for future safety assessments and intelligent monitoring of modern passenger rail systems.

2. Materials and methods

The locomotive model includes a body, 2 bogie frames (including the weight of 4 traction motors), 2 automatic couplers, 2 thrust plates and 4 wheelsets with axle boxes. It should be noted here that in order to speed up the calculation time, the locomotive model does not take into account the power elements and bodies responsible for traction.[9] The passenger wagon model consists of a body, 2 bogie pivot beams, 2 bogie frames, 4 bogie cradles, 2 automatic couplers, 2 thrust plates, 4 buffers and 4 wheelsets with axle boxes. The considered mathematical description of the calculation of the kinematic characteristics of the bodies of the system is implemented in the "Universal Mechanism" complex in the form of a software procedure for specifying a hinge connecting the body under consideration with the base coordinate system (CS). At the preliminary stage, the spatial orientation of the own coordinate system of each body included in the wagon model, parallel to the axes CS_0, is set. In the process of describing the hinges for each body, the vector $r_i^{(0)}$ is specified in the initial position (at t = 0) and the type of orientation angles is chosen.[10] Eq. (1) are solved simultaneously for all bodies within the train-track system, yielding the time-dependent generalized coordinates for linear and angular displacements, velocities, and accelerations. The system of differential equations is integrated using an adaptive Runge-Kutta algorithm within Universal Mechanism, which ensures numerical stability during rapid force transitions occurring in emergency braking.

The equations describing the motion of the i-th body of the mechanical system "car-track" when SCi coincides with the main axes of inertia of the bodies have the form Eq. (1):

$$\begin{cases} m_i \cdot a_{ix}^{(0)} = \sum F_{ix}^{(0)} + \sum R_{ix}^{(0)} \\ m_i \cdot a_{iy}^{(0)} = \sum F_{iy}^{(0)} + \sum R_{iy}^{(0)} \\ m_i \cdot a_{iz}^{(0)} = \sum F_{iz}^{(0)} + \sum R_{iz}^{(0)} \\ J_{ix}^{(i)} \cdot \frac{d\omega_{ix}^{(i)}}{dt} + \omega_{iy}^{(i)} \omega_{iz}^{(i)} \cdot \left(J_{iz}^{(i)} - J_{iy}^{(i)}\right) = \sum M_{ix}^{(i)} + \sum L_{ix}^{(i)} \\ J_{iy}^{(i)} \cdot \frac{d\omega_{iy}^{(i)}}{dt} + \omega_{iz}^{(i)} \omega_{ix}^{(i)} \cdot \left(J_{ix}^{(i)} - J_{iz}^{(i)}\right) = \sum M_{iy}^{(i)} + \sum L_{iy}^{(i)} \\ J_{iz}^{(i)} \cdot \frac{d\omega_{iz}^{(i)}}{dt} + \omega_{ix}^{(i)} \omega_{iy}^{(i)} \cdot \left(J_{iy}^{(i)} - J_{ix}^{(i)}\right) = \sum M_{iz}^{(i)} + \sum L_{iz}^{(i)} \end{cases} \quad (1)$$

where m_i – is the mass of the i-th body, kg; $a_{ix}^{(0)}$, $a_{iy}^{(0)}$, $a_{iz}^{(0)}$ - is the projections of the linear acceleration vector of the i-th body on the global coordinate axes SC_0, m/s^2; $\sum F_{ix}^{(0)}$, $\sum F_{iy}^{(0)}$, $\sum F_{iz}^{(0)}$ – is the sum of the projections of all active forces applied to the i-th body onto the coordinate axes SC_0, N; $\sum R_{ix}^{(0)}$, $\sum R_{iy}^{(0)}$, $\sum R_{iz}^{(0)}$ – is the sum of the projections of all reactive forces applied to the i-th body onto the coordinate axes SC_0, N; $J_{ix}^{(i)}$, $J_{iy}^{(i)}$, $J_{iz}^{(i)}$ – is the moments of inertia of the i-th body about the axes SC_i, kg·m^2; $\omega_{ix}^{(i)}$, $\omega_{iy}^{(i)}$, $\omega_{iz}^{(i)}$ – is the projections of the angular velocity vector of the i-th body on the coordinate axes SC_i, rad/s; $\sum M_{ix}^{(i)}$, $\sum M_{iy}^{(i)}$, $\sum M_{iz}^{(i)}$ – is the sum of the moments of all active forces applied to the i-th body relative to the axes SC_i, N/m; $\sum L_{ix}^{(i)}$, $\sum L_{iy}^{(i)}$, $\sum L_{iz}^{(i)}$ – is the sum of the moments of all reactive forces applied to the i-th body, relative to the axes SC_i, N/m.

It should be noted that the six scalar equations included in the system Eq. (1) are written in different coordinate systems: the first three equations correspond to translational motion and are expressed in the base (mobile) coordinate system, while the last three equations describe rotational motion and are written in the local coordinate system associated with each body.[2] By assembling the systems of Eq. (2) for all rigid bodies forming the train–track model, a global system of second-order nonlinear ordinary differential equations is obtained in terms of generalized coordinates q_i. In compact matrix form, the complete system can be written as:

$$M(q) \cdot \ddot{q}_i + k(q, \dot{q}) = Q \quad (2)$$

where $M(q)$ – is the mass (inertia) matrix of the system; $k(q, \dot{q})$ – is the column vector of generalized inertial and gyroscopic forces that depend nonlinearly on the coordinates and velocities; Q – is the column vector of generalized active forces, including braking, contact, gravity, and damping forces.

The solution of the system of Eq. (2), with respect to the generalized coordinates q_i allows one to determine the linear and angular displacements, velocities and accelerations of the bodies included in the locomotive and passenger wagon

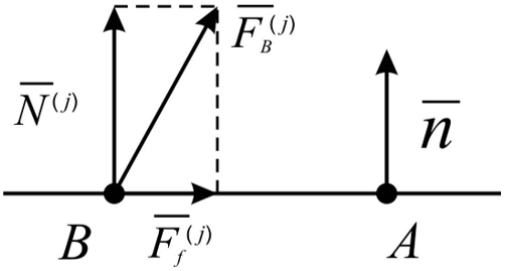


Fig 1: Point-to-plane contact interaction.

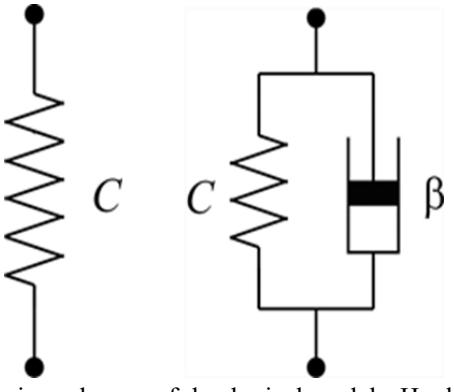


Fig. 2: Design schemes of rheological models. Hooke model.

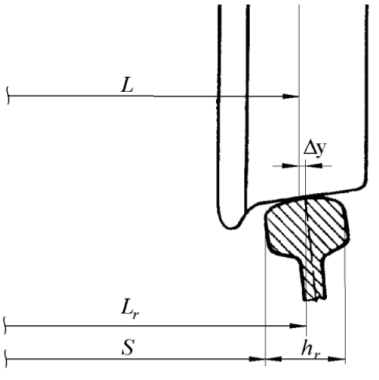


Fig. 3: Rail position in transverse direction. Voigt model.

models. Moreover, it enables the computation of the kinematic parameters of any arbitrary point belonging to these bodies when its position is specified in the local coordinate system of the corresponding component.[11,12] To construct Eq. (2), it is necessary to obtain analytical expressions for the reaction forces in the constraints connecting individual bodies. Power elements in the wagon and locomotive models include: contact interactions between bodies, elastic (spring suspension springs) and elastic-dissipative (dampers) forces.

Contact interaction is used in models to simulate the interaction of side bearings, center plate-thrust center-pivot, and coupler-plate and coupler-auto coupler.[13] When modeling the contact interaction of two bodies, it is assumed that one of the contacting elements is associated with an infinite reference plane, while the other body contains a set of discrete contact points. The degree of local interpenetration (or gap) between the two surfaces is denoted by Δ. If $\Delta \geq 0$, the bodies are separated and no contact forces act between them. If $\Delta < 0$, contact occurs, and a reaction force arises from the reference surface onto the contacting body.

For brevity, only the main representative figures are presented in this section. Extended modeling schematics, rail irregularity patterns, and sensitivity plots are included in the *Supplementary information file* (Figs. S1 – S12). These additional materials support but do not alter the principal conclusions of the study.

This relationship is defined by Eq. (3) (see Fig. 1), which decomposes the contact-reaction vector $\overline{F}_B^{(j)}$ into normal and tangential components:

$$\overline{F}_B^{(j)} = \begin{cases} 0, & \Delta \geq 0 \\ \overline{N}^{(j)} + \overline{F}_f^{(j)}, & \Delta < 0 \end{cases} \quad (3)$$

where $\overline{F}_B^{(j)}$ - is the total contact-reaction vector acting at the j-th contact point; $\overline{N}^{(j)}$ – is the normal reaction vector, directed perpendicular to the contact surface; $\overline{F}_f^{(j)}$ – is the tangential friction force vector.

As illustrated in Fig. 1, the total contact force $\overline{F}_B^{(j)}$ is the vector sum of its normal and tangential components. The normal reaction is governed by a linear elastic-dissipative law, expressed in the local coordinate system SC_j as:

$$N^{(j)} = -\Delta \cdot C_B - \frac{d\Delta}{dt}\beta_B \quad (4)$$

where C_B – is the contact stiffness coefficient at point B; β_B – is the contact dissipation (damping) coefficient at point B.

Eq. (4) thus accounts for both the elastic deformation and the rate-dependent damping at the contact interface. The tangential component $\overline{F}_f^{(j)}$ is described by a Coulomb friction model with two operating regimes-sliding and adhesion (stick).[14] In the sliding mode Eq. (5), the friction force opposes the relative sliding velocity vector $v_S^{(j)}$ and is computed as:

$$F_f^{(j)} = \frac{-fN^{(j)} \cdot v_S^j}{\left|v_S^{(j)}\right|} \quad (5)$$

where f – is the sliding friction coefficient; $v_S^{(j)}$ – is the sliding velocity of one body relative to the other.

When the relative slip velocity $v_S^{(j)}$ approaches zero-indicating no relative motion-the interaction enters the adhesion (clutch) regime. In this mode, the friction force attains its maximum static value Eq. (6), defined by:

$$F_f^{(j)} = -f_0 \cdot N^{(j)} \quad (6)$$

where f_0 – is the static (clutch) friction coefficient.

The numerical algorithm automatically transitions between Eq. (5) and Eq. (6) as the relative slip condition changes sign, ensuring stable simulation of stick–slip phenomena during braking and coupler compression.

Springs, dampers, rods, and other mechanical connections within the locomotive and passenger-car models are

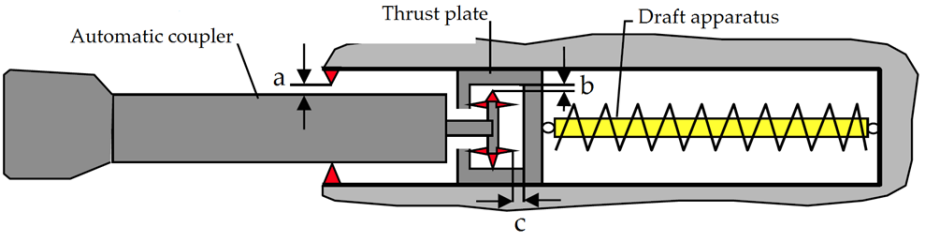


Fig. 4: Coupler model diagram: Automatic coupler; Thrust plate; Draft apparatus; a– clearance between coupler shank and sleeve, b– gap to spring start, c– preload of draft gear.

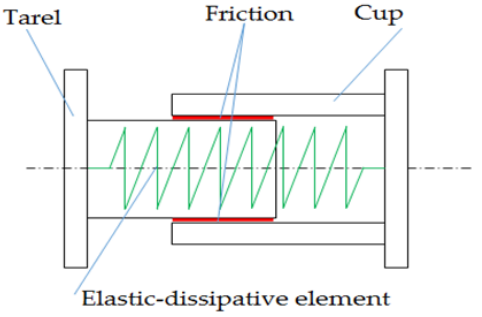


Fig. 5: Scheme of the buffer device model.

represented using elastic and elastic–viscous elements described by the classical Hooke and Voigt rheological models, respectively.[15] These are depicted schematically in Fig. 2 and Fig. 3. The combination of the linear-viscoelastic normal model (Eq. 4) and the Coulomb friction law (Eqs. 5–6) provides an adequate approximation of the nonlinear contact mechanics that dominate the dynamic response of the train during emergency braking.

The elastic components of the suspension system (springs, pivots, rods, and bushings) are represented using linear matrix models that describe the relationships between forces, moments, and corresponding linear and angular deformations.

In the local coordinate system Eq. (7) and Eq. (8) of the elastic element, the force vector F and moment vector M are determined by the following matrix relationships:

$$F = C_r \cdot dR_B^{(A)} \tag{7}$$

$$M = C_\phi \cdot dA_B^{(A)} \tag{8}$$

where C_r – is the linear stiffness matrix of the elastic element; C_φ – is the angular stiffness matrix; $dR_B^{(A)}$ – is the matrix of linear deformation components (relative displacement between points A and B in the local frame); $dA_B^{(A)}$ – is the matrix of direction cosines representing angular deformation between the same points.

Mathematical models of force F_D and moment M_D of an elastic-dissipative element are determined by the following expressions in matrix form:

$$\begin{aligned} F_D &= C_r \cdot dR_B^{(A)} + D_r \cdot d\dot{R}_B^{(A)} \\ M_D &= C_\phi \cdot dA_B^{(A)} + D_\phi \cdot d\dot{A}_B^{A} \end{aligned} \tag{9}$$

where D_r – is the linear dissipation matrix; D_φ – is the angular dissipation matrix.

Eq. (7), Eq. (8) and Eq. (9) thus describe the Hooke-type (elastic) and Voigt-type (elastic–viscous) rheological models, enabling the simulation of both stiffness and damping properties within the bogie suspension, couplers, and buffer systems.[15]

For an ideal, undeformed track, the widening parameter Δy is computed from the geometric difference between the center spacing of the rail heads Lr and the inner spacing of the wheel treads L. The relationship is defined by Eq. (10):

$$\Delta y = \frac{L_r - L}{2} \tag{10}$$

$$\Delta y = \frac{S + h_r - L}{2} \tag{11}$$

where L_r – is the distance between the centers of the rail heads, mm; L – is the distance between the inner wheelset laps, mm; S – is the track gauge (e.g., 1520 mm in the present study); h_r – is the rail head width, mm.

Eq. (10) essentially represents half of the total difference between the wheelbase and the rail-head spacing, reflecting how much the rails are laterally offset from the ideal wheel–rail contact points. When the geometry of the rail head and nominal track gauge are taken into account, the widening can also be expressed using Eq. (11).

In other words, straight track widening is the transverse distance from the lowest point on the wheel's tread circle to the center point of the rail head in their ideal position.[16] Since when the bogies come off, all the wheels lose their contact with the rails, the model included elements that take into account the sliding (rolling) of the wheels on the supporting surface (Fig. S1).

On Fig S2, for convenience of perception, only one interaction option is shown. In fact, the model also implements a symmetrical version of the interaction of the left wheel and the right rail, respectively.[17]

Shown in Fig. S1 and Fig. S2, the schemes for the interaction of wheels with the ground surface and the side faces of the rails make it possible to limit the vertical and lateral movements of the wheels when they are completely derailed.[18]

At the same time, it is assumed that the supporting surface is even, and the resistance to movement caused by the interaction of wheels with sleepers and crushed stone is set by

Table 1: Permissible values of the estimated indicators.

Index		Standard values
Ratio of frame force to static axial load H_P/P_0	Excellent	≤0.20
	Good	0.25
	Satisfactory	0.30
	Permissible	0.38
Lateral forces, *kN*	Permissible	100
Wheel stability factor against derailment λ_{normal}	in direct	1.3

Table 2: Technical characteristics of the rolling stock (accepted for modeling).

Serial number in the train	Container, ton	Length along the clutch axes, m	Base, m	Additional weight from passengers and cargo, ton	Gross weight, ton
Locomotive	-	20.032	10.3	-	85
wagon No.1	55	24.537	17	3.5	58.5
wagon No.2-7, 10, 12	61.5	26.696	19	4	65.5
wagon No.8	58.1	25.5	17	3.5	61.6
wagon No.9	61.5	26.696	19	3.5	65
wagon No.11	61	24.537	17	0.5	61.5
wagon No.13-19	60	26.696	19	6	66
wagon No.20	51	24.537	17	6	57

additional forces applied to the wheelsets.[19] In order to take into account the longitudinal forces between the cars, automatic couplers and buffers were added to the model (see Fig. 4 and Fig. 5).

The automatic coupler is represented by a nonlinear spring-damper assembly consisting of a coupler shank, a thrust plate, and a draft apparatus containing an energy-absorbing spring (Fig. 4). This configuration allows simulation of both traction (tension) and compression (buffering) phases during sudden braking. The coupler system exhibits nonlinear stiffness, since the internal gaps a, b, and c define distinct regions of free motion followed by progressive compression of the buffer spring. This behavior reproduces the impact absorption and load-transfer delays that occur when adjacent cars undergo sudden deceleration.

Braking forces were implemented using a moment tending to turn the wheel in the opposite direction (or stop the wheel) defined by the expression:

$$M_b = 4F_f \cdot r_k = 4F_p \cdot \varphi \cdot r_k(r_\partial) \qquad (12)$$

where F_f – is the frictional force between the wheel and the brake block, kN; F_p – is the pressing force acting on one brake pad, kN; φ – is the coefficient of friction between the wheel and rail; r_k – is the radius of the wheel, *m*; r_∂ - is the relative radius of the frictional contact point.

Eq. (12) thus expresses the braking moment as the total torque resulting from the four brake shoes acting on each wheelset (two per side), multiplied by the effective radius of force application. This formulation captures the deceleration effect on both rotational and translational motion during braking.

The buffer apparatus acts as a shock absorber, dissipating the kinetic energy of coupler compression through combined elastic and frictional mechanisms. Its design is schematically illustrated in Fig. 5, where the spring and friction elements are connected in a Voigt-type rheological configuration. This model ensures a realistic representation of energy dissipation during coupler compression. The spring element stores energy elastically, while the frictional interfaces convert part of it into heat, reducing shock loads transmitted to adjacent vehicles. The internal structure of the buffer's elastic-dissipative element is shown in Fig. S3, consisting of two cups enclosing a spring and friction plates.

The pressing force per brake shoe F_p in Eq. (13) is determined from the brake-cylinder pressure and the mechanical linkage ratio according to the following relationship:

$$F_p = i \cdot \frac{\eta\left(p_{cy} \cdot S \cdot \eta_{cy} - F_{sp}\right)}{n_k} \qquad (13)$$

where i – is the gear ratio of the brake linkage, taken as 12 for passenger wagons equipped with cast-iron brake blocks;[6] η and η_{cy} – are the efficiencies of the brake linkage and brake cylinder, assumed to be 0.95 and 0.98, respectively; S – is the piston area of the passenger wagon brake cylinder is 0.0993 m^2; F_{sp}– is the release spring force 2473 N; p_{cy} – is the pressure in the brake cylinder, Pa, determined from the brake-filling indicator diagram (Fig. S4).

Eq. (13) thus provides the effective normal force transmitted through the brake linkage to each pad, accounting for mechanical and pneumatic losses. The product of F_p and the friction coefficient φ determines the tangential braking force, which ultimately influences the braking distance and

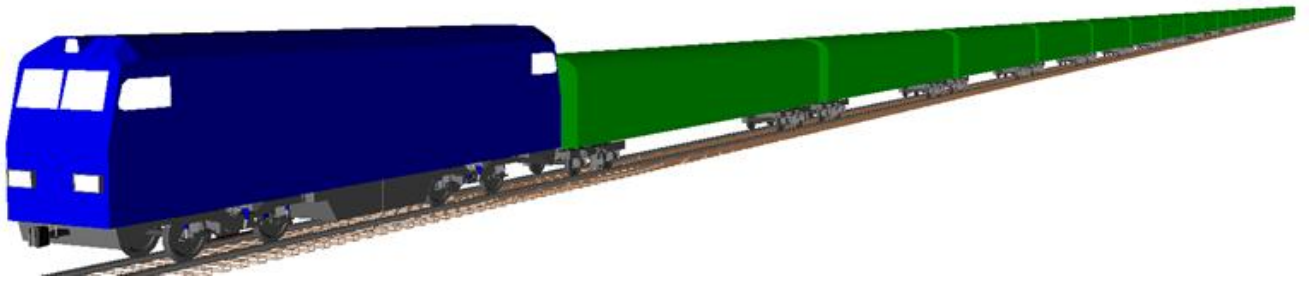


Fig. 6: General view of the train model.

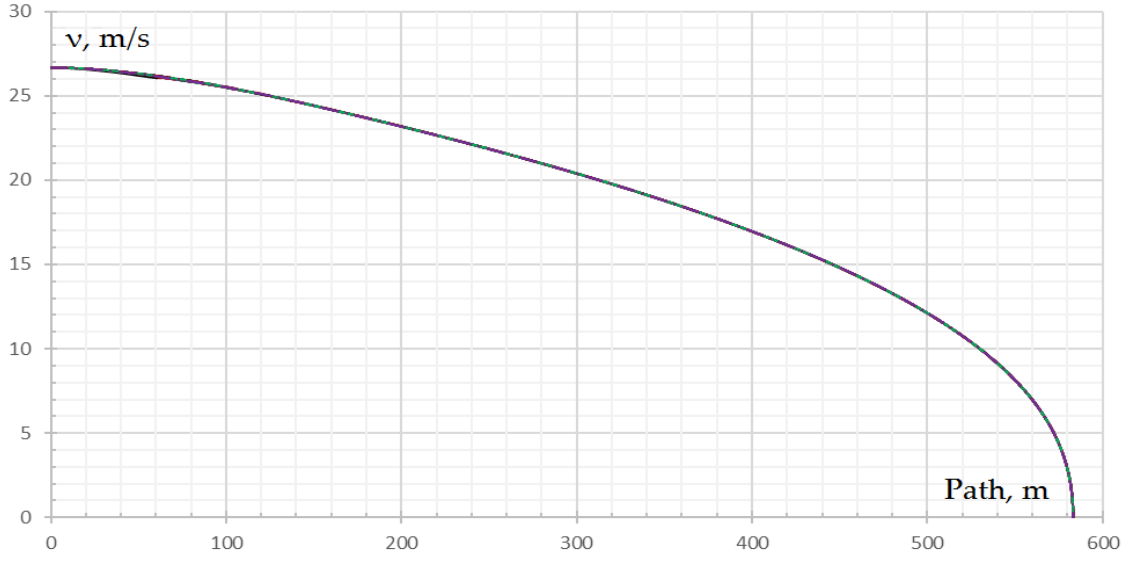


Fig. 7: Graph of the decrease in the speeds of the rolling stock units of the train during braking.

coupler compression dynamics.

According to operational data, the average filling time of the brake cylinders in passenger cars was measured as 5.7 seconds. The pressure increase within the cylinder over time follows the empirical filling curve shown in Fig. S4, representing the transient build-up of braking force in response to driver activation of the emergency braking mode. This time-dependent pressure function $p_{cy}(t)$ is incorporated into the model to ensure accurate simulation of non-instantaneous braking and to reproduce the propagation delay of the pneumatic brake wave along the 20-wagon train consist.[20]

Using Eq. (13), the pressing force on one brake shoe was determined from the measured $p_{cy}(t)$ values. The resulting curve of brake-shoe pressure versus time is presented in Fig S5, illustrating the gradual increase of normal force as the brake cylinder fills. The curve demonstrates that the brake pressure builds up smoothly to its maximum of about 27 N after 6 s of actuation.

Using expression Eq. (13), authors determine, in accordance with the filling diagram of the brake cylinder,[21] the values of the pressing force on one brake shoe and build a brake pressure diagram (see Fig. S5). The coefficient of friction between the cast-iron block and the wheel is determined by the expression for a constant value of the pressing force:[22]

$$\phi = 0{,}6\frac{1.6F+100}{8F+100}\cdot\frac{v+100}{5v+100} \quad (14)$$

where F – is the pressing force, kN; v – is the train speed, km/h.

Eq. (14) indicates that φ decreases rapidly with increasing v, which agrees with experimental adhesion data. The resulting trend, shown in Fig. S6, demonstrates a rapid decline of ϕ from 0.25 – 0.30 at low speeds to below 0.10 at 100 km/h, consistent with published adhesion data for conventional cast-iron blocks. For locomotives such as the KZ4AC model, equipped with disc-type brakes, the braking torque $4F_p\varphi r_d$ in Eq (12) is applied through the radius of the middle brake disk r_∂ instead of the wheel radius r_k.[23] The coefficient of friction between the composite pad and the wheel tread is determined empirically by:[7]

$$\phi = 0.44\frac{F+20}{4F+20}\cdot\frac{v+150}{2v+150} \quad (15)$$

where F – is the pressing force, kN; v – is the train speed, km/h.

The corresponding dependence is plotted in Fig. S8, which shows a smoother decrease of friction with speed than that of cast-iron pads, confirming their better thermal stability and consistent performance under high-speed braking. Together with Eq. (12), Eq. (13), Eq. (14) and Eq. (15), these relationships enable a realistic simulation of combined braking

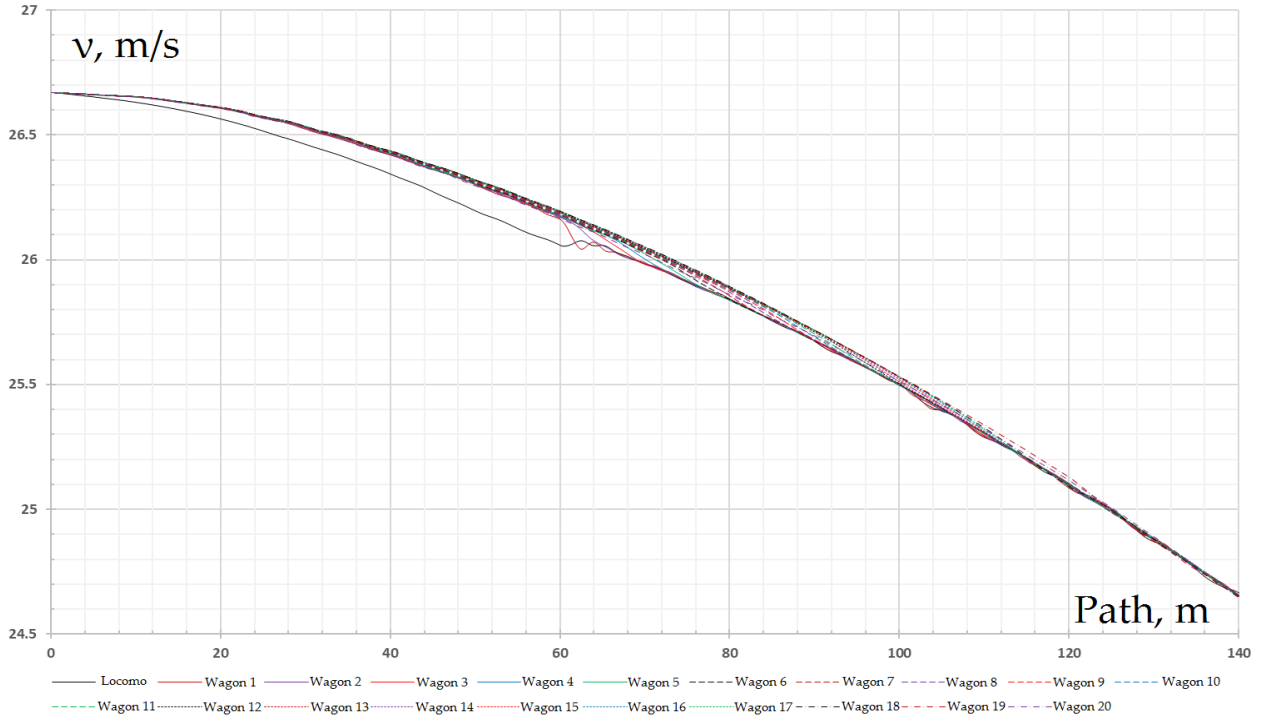


Fig. 8: Graph of deceleration of train rolling stock units (transient process).

and rolling-resistance effects, thereby ensuring that both pneumatic dynamics and mechanical resistances are faithfully reproduced in the virtual test environment.

The total braking pressure acting on a locomotive wheelset axle, computed from the superposition of brake-shoe forces, is shown in Fig. S7. This diagram was derived from the operational data of a KZ4AC electric locomotive by decoding its onboard recorder. It illustrates how the braking pressure stabilizes after approximately 10 s of actuation, reaching ~210 N per shoe.

In accordance with the traction-calculation standards,[6] the specific rolling resistance of a passenger wagon on a seamless track is expressed as:

$$W_{wagon} = 0.7 + \frac{8+0.16\nu+0.0023\nu^2}{q_0} \quad (16)$$

where $q_0 = \frac{m_{wagon}}{4}$ – is the axle load in tons. m_{wagon} – is the average weight of a fully equipped wagon is assumed to be 64.475 tons.[24]

Similarly, for the locomotive operating in coast-down mode, the specific resistance on a seamless track is determined as:

$$W_{locomotive} = 2.4 + 0.009\nu + 0.00035\nu^2 \quad (17)$$

where ν is the train speed (km/h).

These empirical expressions Eq. (16) and Eq. (17) are essential for calculating the total braking deceleration, as they represent the resistive forces opposing motion even in the absence of active braking.

The dependences in Fig. S9 illustrate that the specific resistance of both wagons and locomotives increases nonlinearly with velocity, primarily due to the aerodynamic drag component represented by the quadratic term in Eq. (16) and Eq. (17).

For the wagon, the total specific resistance W_{wagon} increases from about 1.1 to 3.7 as the velocity increases to 100 km/h, reflecting the influence of aerodynamic drag and rolling friction (Fig. S9). By performing elementary transformations of those expressions, we obtain the corresponding force-based formulations:

$$W_{wagon} = g \cdot \left(0.7 + \frac{8+0.16\nu\cdot 3.6+0.0023(\nu\cdot 3.6)^2}{q_0}\right)\frac{m_{wagon}}{1000} \quad (18)$$

$$W_{locomotive} = g \cdot (2.4 + 0.009\nu \cdot 3.6 + 0.00035(\nu \cdot 3.6)^2)\frac{m_{locomotive}}{1000} \quad (19)$$

where g – is the gravitational acceleration, m/s^2; ν – is the train speed, m/s; m_{wagon} and $m_{locomotive}$ – is the respective vehicle masses, kg; q_0 – is the axle load, t.

Eq. (18) and Eq. (19) thus provide the total resistance force in N, which is then applied in the simulation model at the center of gravity of each rolling-stock unit, directed opposite to the direction of motion.[25] After converting to physical units via Eq. (18) and Eq. (19), the resistance dependences were plotted in N as functions of speed, as shown in Fig. S11 and Fig. S12. These relationships quantify the actual braking-opposing forces acting on the rolling stock.

Dependences of the dimensionless and recalculated in Newton's of the main specific resistance of movement on speed are shown in Figs. S10-S12. Forces that simulate resistance to movement are applied to the centers of gravity of

Table 3: Conditions for carrying out numerical experiments.

S. No.	Name	Meaning	Unit
1.	Path microgeometry	Straight	-
2.	Vertical stiffness per rail	50	MN/m
3.	Transverse stiffness per rail	20	MN/m
4.	Vertical dissipation per rail	800	kN/m
5.	Transverse dissipation per one rail thread	320	kN/m
6.	Rail profile	New P65	
7.	Wagon wheel profile	New	
8.	Modulus of elasticity in wheel-rail contact	$210*10^9$	N/mm^2
9.	Poisson's ratio in wheel-rail contact	0,27	
10.	Coefficient of friction between wheel and rail	0,25	
11.	Travel speed	96	km/h
12.	Wagon base	19	m
13.	Wagon gross weight	65,5	ton
14.	The distance between the extrema of two small waves of irregularity of type 1	6; 9; 14	m
15.	The distance between the extrema of two adjacent waves of irregularity of type 2	6; 12; 18	m

each unit of rolling stock and are directed against the direction of movement.[25]

For the locomotive, the total specific resistance $\boldsymbol{W}_{\text{locomotive}}$ grows from ≈ 2.4 to 7.0 in the same velocity range, as shown in Fig. S10, which corresponds to its higher mass and greater aerodynamic cross-section. As shown in Figs S11-S12, the resistance force acting on a single wagon grows from approximately 600 N at 5 m/s to over 2200 N at 27 m/s, while for the locomotive, the force rises from about 2000 N to 5600 N in the same range. These values were incorporated into the train model as distributed resistive forces acting along the consist to simulate realistic traction–braking transitions.

In the present model, both the wheel and rail profiles were assumed to be new and conforming to the standard R65 and ER9 geometries, respectively. This assumption simplifies contact-geometry computation and ensures that the derived forces depend only on kinematic and dynamic parameters. However, wear-induced deviations in flange thickness, tread conicity, and railhead shape-especially after multiple emergency braking cycles-can significantly alter the wheel-rail contact patch, tangential creep forces, and rolling radius difference. These effects were not included in the current simulation and may lead to underestimation of the lateral and longitudinal contact stresses over long-term operation.

3. Results (motion simulation)

The theoretical model developed in Section 2 serves as the physical and mathematical foundation for the subsequent numerical simulation in Universal Mechanism. Although the commercial software provides an integrated multibody environment, its dynamic core relies on the same equations of motion and force relations formulated in Section 2. Therefore, the analytical derivations are not repeated in UM but are used to parameterize and validate the simulation model. In particular, the expressions for longitudinal and buffer forces, damping ratios, and coupling stiffnesses derived earlier define the input parameters and provide theoretical limits against which the numerical results in Section 3 are compared. Experimental studies and modeling of the behavior of railway vehicles in the braking mode have been given attention by various authors.[2] Before modeling the movement of the entire train, which takes significant computing resources, a series of calculations was carried out using single models.[26] At the same time, longitudinal and braking forces were not taken into account at this stage, since their influence on an individual crew is very small. When determining the causes of rolling stock derailment, as a rule, the main criterion to be assessed is the wheel derailment stability factor (the tendency of the wheel to "crawl" with the flange onto the rail head), which is based on the consideration of the wheel balance equations under conditions of contact with the flange:

$$\lambda = \frac{tg\beta - \mu}{\mu \cdot tg\beta + 1} \cdot \frac{P_{ver1}}{P_{hor}} \geq [\lambda_{normal}] \qquad (20)$$

where β – is the inclination angle of the wheel's conical surface generatrix relative to the horizontal plane, rad; μ – is the coefficient of friction between the wheel and rail contact surfaces; P_{ver1} – is the vertical component of the wheel–rail contact reaction, N; P_{hor} – is the horizontal component of the reaction force, N; $[\lambda_{normal}]$ – is the admissible stability coefficient, defining the safe margin against derailment.

Eq. (20) thus provides the quantitative measure of flange climbing risk: derailment is possible when $\lambda < [\lambda_{normal}]$. This expression is widely adopted in UIC and EN 14363

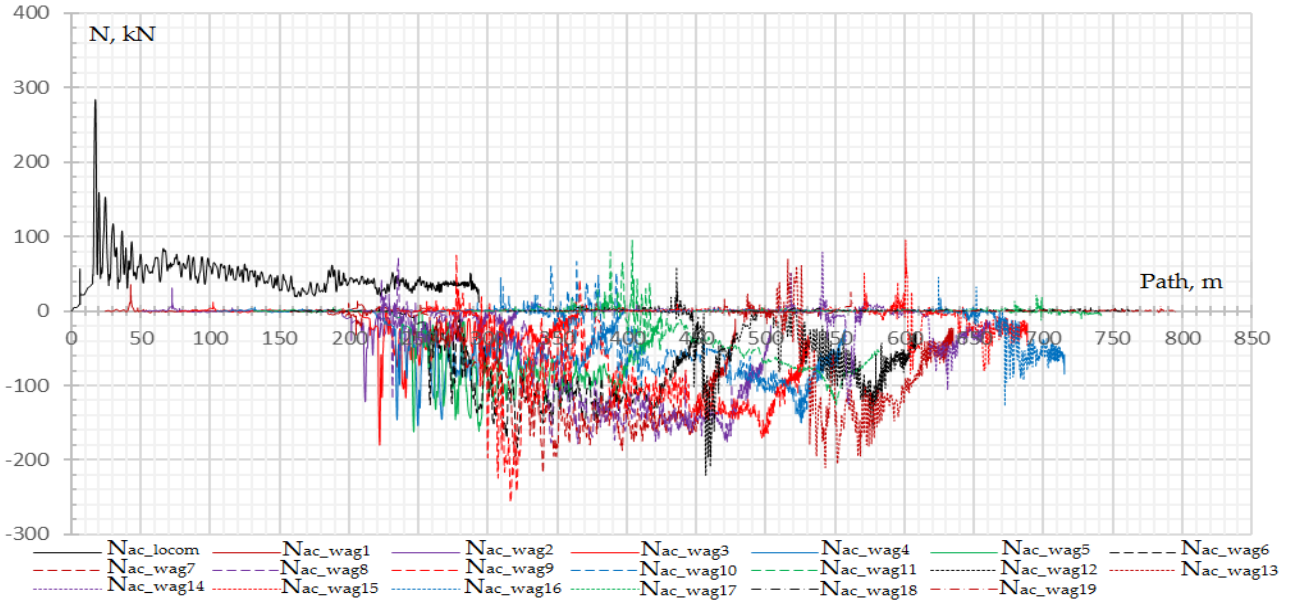


Fig. 9: Longitudinal forces on the tail couplers of the locomotive and wagons (option No. 1).

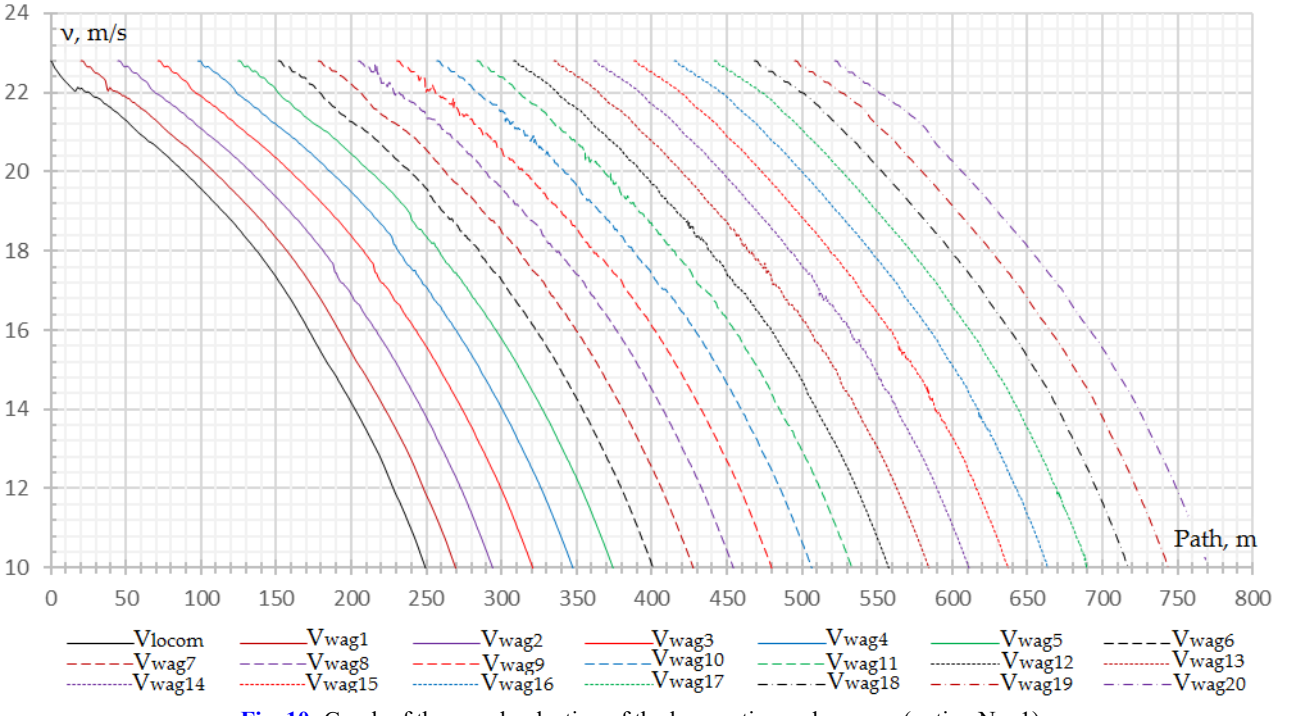


Fig. 10: Graph of the speed reduction of the locomotive and wagons (option No. 1).

standards for evaluating running safety and dynamic stability of rolling stock under various operational conditions.

Lateral and frame forces are also important indicators that evaluate the force effect of the crew on the track. Exceeding the normative values of these forces can cause the destruction of the track and the derailment of the crew.[27] The maximum allowable values of frame forces are calculated from the condition of stability of the rail-sleeper grid of the track from transverse shear along the ballast under the influence of the frame force as the ratio of the frame force $H_p k$ to the axial load P_0 (H_p/P_0). Normalized values of the mentioned indicators are given in Table 1.

Supplementary information file Figs. S13-S30 and Tables S1-S4 provide the full oscillograms of longitudinal and frame forces for all train configurations and braking scenarios. To calculate the lateral forces, the totality of all forces acting on the wheel during contact interaction with the rail at all points of contact is used. In addition, when analyzing wheel derailment, the transverse displacements of wheelsets relative to the track axis are additionally evaluated.[28] It is obvious that, due to the increased inertial parameters, the locomotive will definitely pass, without rolling the wheels onto the rail head, the irregularities, during the passage of which the passenger wagon will derail. In this regard, the simulation of the situation of the derailment of the locomotive was not carried out. At the same time, assuming that the effect of vertical irregularities on

horizontal oscillations is insignificant, vertical irregularities with an "excellent" rating were used in the calculations. The numerical values of the irregularities taken by the track measuring wagon for 1500 km of the considered section of the track are shown in Fig. S13. As seen in Fig. S13, the horizontal irregularities fluctuate within ±10 mm, with small-scale wavelength components corresponding to sleeper spacing and longer harmonic deviations reflecting track geometry variations. These data were used to excite the vehicle–track interaction model in the Universal Mechanism environment, ensuring that the simulated motion accurately represents the dynamic response of the rolling stock to real-world track conditions.

As shown in Fig. S14, both the left and right rails exhibit similar oscillatory behavior, with phase-shifted deviations of up to ±8–10 mm. These variations generate alternating lateral excitation forces that are transmitted to the wheelsets and bogie frames, resulting in transverse vibration modes that significantly affect ride stability and derailment risk. Such measured irregularities were incorporated into the Universal Mechanism simulation environment as input excitation data for the coupled "track-vehicle" system. This approach ensures that the simulated braking process accurately reproduces the real-world dynamic loading conditions, including the influence of track geometry imperfections on the wheel–rail interaction.

To ensure that the input geometry data for the simulation accurately reflect real track conditions, the horizontal roughness of the rail threads was analyzed for different time periods. Fig. S15 and Fig. S16 illustrate the lateral irregularities of the right and left rail threads, respectively, recorded in May and June, over a 200 m representative section of the same 1500 km track segment. As can be observed in Fig. S15 and Fig. S16, the amplitude of deviations in both the left and right rail threads does not exceed ±8 mm, indicating high-quality track alignment. The measured phase similarity between the May and June data confirms the stability of the geometric condition of the track during this monitoring period. Small differences in the waveforms correspond to minor seasonal variations in ballast stiffness and rail–sleeper settlement, which were automatically included in the model's excitation profile. For simplification, the simulations were carried out using the track geometry corresponding to the months of May and June, as these periods exhibit minimal external interference from climatic effects. However, in future studies, the simulation framework can be extended to autumn and winter conditions, where rainfall, snow accumulation, temperature gradients, and frost heave alter both the adhesion coefficient and wheel–rail contact geometry, thereby influencing lateral dynamics and derailment probability.[28]

To assess the temporal variability of track geometry, Fig S17 shows the change in the amplitudes of the rail thread irregularities over the course of one month. Here, the negative values correspond to a reduction in roughness amplitude, which reflects track stabilization or partial settlement of ballast after maintenance works. The analysis of these variations is important for understanding seasonal deformation patterns and their influence on wheel–rail contact forces during braking.

From Fig. S15, Fig. S16, Fig. S17 and Fig. S18, it can be seen that the periods of lateral irregularities acting on the 1st–2nd wheelsets fall mainly within the range of 5–14 m. In addition, a clear phase mismatch between the left and right rail threads is observed in the segment between 160–190 m, as shown in Fig. S18. This asymmetry can lead to differential excitation of the wheelsets, resulting in lateral oscillations, increased flange contact, and consequently a higher risk of derailment in the event of strong braking or external disturbances.

Based on a Comprehensive Pre-Failure Analysis (CPFA) of the track condition using the Seamless Path (SP), Resource Management, Risk Management, and Reliability Analysis (RMMRA) software suite, it was found that at the 2nd–3rd wheelsets, temperature-induced stresses caused localized unevenness in the track alignment. According to studies,[6–8] such irregularities in straight track sections can be mathematically represented by the fading roughness functions shown in Fig. S19 and Fig. S20.

These theoretical profiles describe smooth periodic deformations with gradually decreasing amplitude, which are typical of temperature-induced buckling waves or settlement effects in continuously welded rails. Such imperfections produce localized excitation zones, where transient vertical-lateral coupling forces may cause an increase in the wheel unloading ratio or reduction in flange safety margin. It is clear that the sudden braking or derailment process cannot be reproduced in full using numerical simulation alone, since numerous interdependent factors influence the actual event-such as the time-dependent shape variation of irregularities under temperature changes, elastic–plastic deformation of the ballast, and vehicle-track feedback effects. Therefore, a reliable understanding of the derailment process requires a combined deductive–inductive approach, integrating both computational simulations and local model analyses of specific mechanical subsystems of the rolling stock and the track.[29] Such a hybrid approach enables the identification of the key influencing factors and their contribution to overall train dynamic stability and safety.

Based on the parameters summarized in Table 2, a comprehensive train model was created in the Universal Mechanism simulation environment. The modeled consist includes a locomotive and 20 passenger wagons, coupled through automatic couplers and draft gear devices, operating under the track irregularities presented earlier in Figs. S13–S18. The geometric layout and structural configuration of the train are shown in Fig. 6.

Using the developed train model Fig. 6, the emergency braking process was simulated by applying a sudden braking moment on all wheelsets simultaneously, in accordance with the braking force distribution law given in Eq. (12), Eq. (13),

Eq. (14) and Eq. (15). The braking distance was determined by integrating the velocity-distance relationship for each rolling stock unit. Fig. 7 presents the deceleration curve of the locomotive and wagons as a function of the distance traveled after the onset of emergency braking. The total braking distance was 583 m, measured from the moment of brake application until full stop. This result falls within the acceptable range established by current railway safety standards (MFI),[6] confirming the adequacy of the model and braking system parameters. A magnified view of the transient phase of velocity reduction - representing the moment of coupler tightening and initial dynamic response of the train - is shown in Fig. 8. This region corresponds to the time interval when the buffer and draft apparatuses undergo compression, damping the shock wave propagation through the train formation.[30]

The longitudinal forces acting between adjacent rolling stock units were calculated over the braking process. Figs. S21–S25 show the oscillograms of total longitudinal forces between neighboring vehicles as functions of the distance traveled. The simulation results indicate that,[31] owing to the presence of buffer devices and elastic–dissipative couplers, the braking process remains smooth and shockless for most of the train. However, the maximum transient force peak occurs at the connection between the locomotive and the first wagon, where the highest dynamic loads arise due to the inertia mismatch between the heavier locomotive and the lighter leading wagon. The propagation of these forces along the train length demonstrates a damping trend, confirming that the elastic–viscous couplers efficiently dissipate the initial compression impulse. This ensures that subsequent wagons experience significantly reduced force amplitudes, thereby preventing damage to coupler mechanisms and minimizing longitudinal oscillations.[32]

The total longitudinal interaction force between the rolling stock units during braking is defined as the sum of the forces in the automatic coupler and the forces transmitted through the buffer devices of the wagons. This total force was calculated according to the following expression:

$$N_{sumi} = N_{ACi} + \sum N_{bi} \quad (21)$$

where N_{ACi} – is the longitudinal force in the tail coupler of the i-th rolling stock unit, N; $\sum N_{bi}$ – is the sum of the longitudinal forces acting in the tail buffer devices of the wagons, N.

Eq. (21) makes it possible to describe the distribution of internal forces throughout the train composition and to identify the most stressed sections during sudden braking, coupler tightening, or elastic compression of the formation. The inclusion of both coupler and buffer forces provides a comprehensive assessment of the longitudinal load path,[33] accounting for the combined effects of elastic deformation and energy dissipation within the draft gear system. This relationship allows one to obtain the instantaneous total load transmitted through each coupling during the dynamic braking process and to assess both compression and tension phases that arise along the train formation.[34]

The mathematical relationships derived in Section 2 were fully incorporated into the Universal Mechanism model through appropriate mass–inertia definitions, joint constraints, elastic-dissipative force elements, and measured track-irregularity inputs. Each analytical expression Eqs. (1–21) corresponds to a specific modeling block or parameter in UM, ensuring that the numerical simulation reproduces the full longitudinal–lateral–vertical coupling of the train–track system.[35]

Analysis of the simulated oscillograms (Figs. S21–S25) showed that the transient compression process of the train formation occurs during the first 150 m of braking. Within this initial segment, all coupler slack is eliminated, and the draft apparatuses experience elastic compression and subsequent damping. After this point, the process enters a steady dynamic equilibrium, characterized by smooth propagation of elastic deformations and stabilized longitudinal stresses along the train. As illustrated in Fig. S26, the last wagon, owing to its reduced mass, exhibits a slightly delayed velocity response compared to the preceding wagons. This lag produces a tensile phase in the coupler forces between the last and penultimate wagons, confirming that the wave of compression-tension alternation extends throughout the consist. Nevertheless, the amplitude of these tensile peaks remains within allowable dynamic limits, indicating no risk of coupler failure or detachment.

At the next stage, a comparative evaluation of the frame forces acting on wagon bogies was performed during the braking and coasting (run-down) modes along a 500 m track section. These forces, which characterize the lateral dynamic impact of the rolling stock on the rail–sleeper grid, are crucial for determining track stability and derailment safety. The oscillograms (Figs. S27–S30) show that the frame forces are significantly lower in braking mode compared to the coasting mode. In the graphs, dashed lines represent the coasting regime, while solid lines correspond to braking conditions.[36] The reduction in lateral forces during braking can be explained by the stabilizing influence of longitudinal deceleration, which suppresses lateral oscillations of bogies and reduces flange contact intensity. Thus, the numerical results confirm that wagon derailment could not have been caused by lateral displacement of the rail–sleeper grid under braking, since the frame forces remain below the critical threshold for ballast shear. Furthermore, these findings validate the dynamic stability of the simulated train formation and the adequacy of its coupler-buffer damping system.

Before simulating the derailment scenarios, a set of numerical experiments was carried out to study the influence of track irregularities, wheel–rail contact parameters,[37] and dynamic characteristics of the rolling stock. The computational model incorporated the full geometry of the train (locomotive + 20 wagons) and the detailed representation of the wheel–rail interaction under braking and coasting modes. The initial parameters and boundary conditions

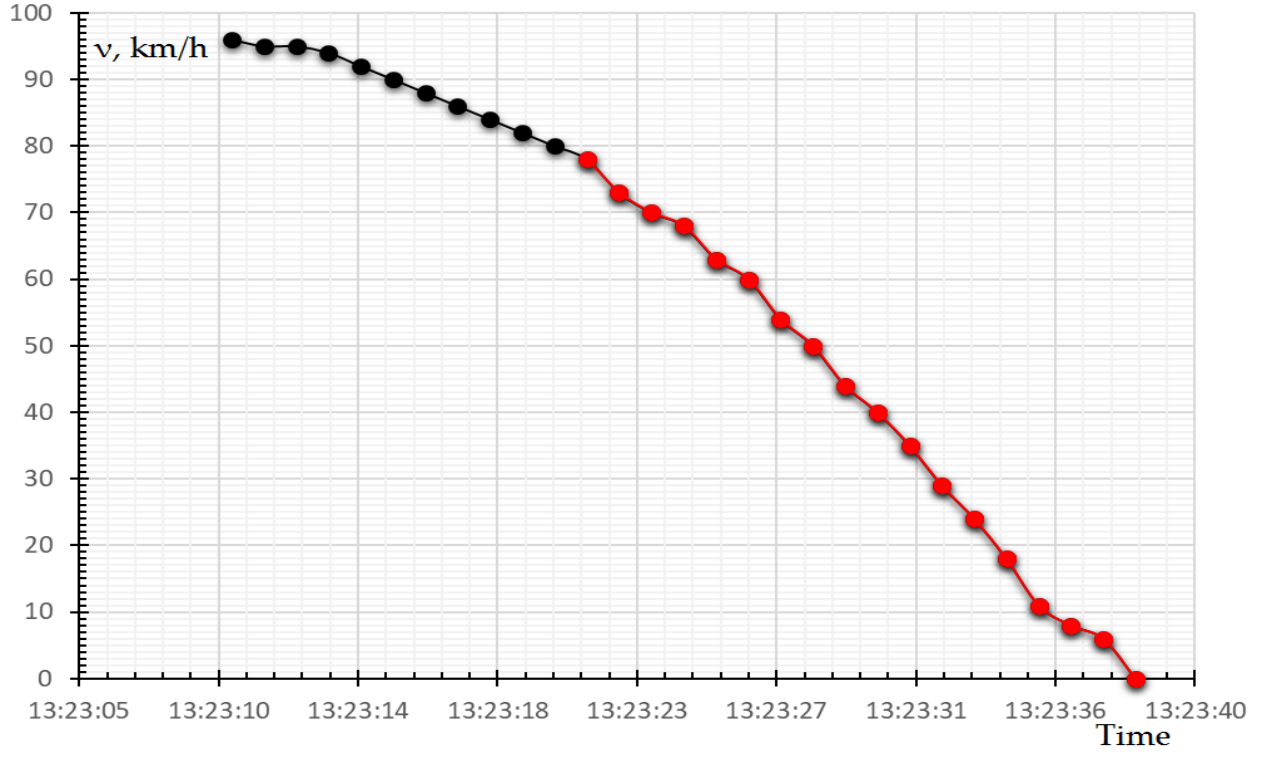


Fig. 11: Graph of deceleration versus time during braking.

adopted for the simulations are summarized in Table 3.

Tables S1 and Table S2 show the roughness values at which wheels derailment is possible. The next stage of the study involved determining the critical values of track roughness that could potentially lead to wheel derailment during emergency braking or motion along irregular sections of the track. The results of this numerical investigation are presented in Tables S1 and Table S2, which list the combinations of amplitude *a* and wavelength *l* of unevenness for which derailment is possible for different wheelsets of the wagon.[38]

From the data given in Tables S1 and Table S2, it can be seen that for a single unevenness of type 1, wheel derailment is possible at values *a*=95-100 mm, L=6 m, and for a double-sided unevenness of type 2 at *a*=80 mm, L= 6 m.

At the same time, the behavior of the wagon is noticeably different with the right and left irregularities.[12] An analysis of the longitudinal forces in the tail couplers and the total longitudinal forces of the tail couplers in the buffers of the locomotive and wagons showed that the forces of additional resistance to the movement of the train, arising after the derailment of the wheels, contribute to the gradual emergence of tensile forces in the automatic couplers of the front cars.[16] With options no. 1 and no. 2, the longitudinal tensile effect does not reach the locomotive, and with option no. 3, the tensile effect reaches the locomotive 150 meters after the possible exit of wagon no. 8, which corresponds to the passage of wagons no. 13-14 of the place of possible exit.

Tables S1 and Table S2 define the parameter domains used to assess the derailment risk under roughness types 1 and 2. However, for brevity, the present paper lists only the amplitude-wavelength grid. The complete numerical values of the derailment coefficient λ and wheel unloading ratios for all combinations of (a, l, wheelset) were obtained from the UM simulations[34] and are provided in *Supplementary information file* Table S3. In the analyzed cases, derailment occurred when $\lambda \geq 1$ and vertical force dropped below 0.05 P_0. The critical combinations correspond to a = 95–100 mm, l = 6 m for type 1 and a = 80 mm, l = 6 m for type 2 roughness.These results confirm the thresholds stated in Section 3 and provide reproducible quantitative criteria for derailment prediction. To assess the dynamic interaction of rolling stock units during emergency braking and under derailment conditions, the simulation results were analyzed for three derailment scenarios (Options No. 1–3). Fig. 9 and Figs. S31-S35 show the oscillograms of the longitudinal forces acting in the automatic couplers and buffer devices along the train formation, depending on the traveled distance. The graphs in Fig. 9 and Figs. S31-S32 represent the variation of the axial (coupler) forces N_{AC} along the train for each wagon and the locomotive.

In Option No. 1, the oscillograms show a sharp transient compression phase in the first 150 m of motion, after which the forces stabilize around the mean negative value (compression). The maximum compressive forces reach about 300 kN at the front of the train (locomotive-wagon 1 interface). In the middle wagons, the forces attenuate due to the elastic-dissipative behavior of the couplers and buffers.[39]

In Option No. 2, the amplitude of oscillations increases, and force reversals are observed around 400–600 m, indicating zones where tensile stresses appear as the couplers extend after

initial compression. This effect is particularly pronounced in wagons 8-12, corresponding to the simulated derailment section.

In Option No. 3, the tensile forces propagate further, reaching up to 600 kN between wagons 13–14 and extending to the locomotive (150 m after derailment initiation). This confirms that loss of wheel–rail contact and the resulting additional resistive forces cause longitudinal shock transmission through the entire train length.

Figs. S33–S35 show the total longitudinal forces acting in the buffer devices of all wagons, N_{buff}, as functions of the traveled path. In Option No. 1, the buffers primarily experience compressive damping, with forces not exceeding 250 kN, indicating shockless braking and effective energy absorption. The system behaves stably with only small transient peaks in the first 300 m. In Option No. 2, due to stronger dynamic coupling between wagons, periodic compression-rebound cycles occur, and the force envelope broadens to 300 kN. This corresponds to a more pronounced elastic wave propagation along the train body. In Option No. 3, the total buffer forces reach 350–400 kN, with evident high-frequency oscillations caused by the derailment-induced traction-compression transition. The rear wagons show delayed oscillation phases, consistent with wave propagation and dissipation phenomena.

The delay in the force response between adjacent wagons confirms the sequential propagation of longitudinal impacts through the coupler chain.[40] Wagons near the locomotive exhibit smoother and lower-magnitude variations (below 250 kN), whereas the middle section of the consist, especially wagons 8–10, shows the most pronounced fluctuations. These dynamics demonstrate that the central part of the train is subjected to the highest transient stresses during sudden braking, emphasizing the role of buffer devices in attenuating shock transmission. Additional simulation results for different braking intensities and track irregularities (see *Supplementary information file* Figs. S31–S35) show similar trends but with varying magnitudes of compressive–tensile transitions depending on coupler stiffness and brake propagation delay.

This behavior arises because, after the possible derailment of the 3rd and 4th wheelsets of wagon No. 8 and subsequently all wheelsets of wagon No. 9, the following sequence occurs:

- The rear wagons, still maintaining contact with the rails, continue to move forward, running into the derailed wagons and producing compressive forces.

- Simultaneously, the front wagons (closer to the locomotive) continue moving at a slightly higher velocity, generating tensile forces in the couplers.

- This dual process-compression from the rear and tension from the front-explains the alternating oscillations observed in the total longitudinal force diagrams.

To illustrate this process more clearly, Fig. 10 and Fig. 11 and Fig. S36 and Fig. S37 show the results of numerical simulation of speed reduction for the locomotive and each wagon in the train during emergency braking.

To ensure the reproducibility of the numerical results, key simulation data have been summarized in Table S3. These include maximum and minimum coupler and buffer forces, velocity and acceleration extrema for each wagon, and braking-distance statistics for all test scenarios. The full time-series datasets and track-geometry inputs are available in the supplementary material. This enables independent verification and facilitates future meta-analyses or comparative studies using other dynamic simulation environments.[41] A condensed summary of the principal numerical results, including braking distances, maximum coupler and buffer forces, and mean wagon velocities for all modeled irregularity scenarios, is provided in Table S4 to facilitate reproducibility and independent verification.

4. Conclusion

This section is not mandatory but can be added to the manuscript if the discussion is unusually long or complex. Equations have been made that allow one to determine the linear and angular displacements, velocities and accelerations of the bodies included in the wagon model, as well as any points belonging to the bodies, when specifying their position in the coordinate system of the corresponding body.

To study the mode of sudden braking of a passenger train, a computational model of the longitudinal dynamics of the train is proposed, which is a chain of solid bodies connected by nonlinear links that take into account the state in each connection and its characteristics, including gaps.

This study developed a detailed dynamic model of a full passenger train (locomotive + 20 wagons) to analyze longitudinal, lateral, and vertical dynamics during emergency braking using the Universal Mechanism software environment. The modeling results allowed estimation of braking distance (≈ 583 m), coupler and buffer interaction forces (245-598 kN), and wagon velocity distributions, as summarized in Table 7 (see Supporting Information). Simulation of different irregularity scenarios (Options 1–3) revealed that derailment risks primarily occur at unevenness amplitudes a>80–100 mm with short wavelengths L<6 m, and that post-derailment tensile effects propagate only partially through the train formation.

Using the generated model as an example, the calculated braking distance of the train was determined and an analysis of the longitudinal force between the automatic couplers of adjacent wagons was carried out, under the condition of the track with random irregularities.

The use of sudden braking can cause derailment of passenger wagons under certain circumstances discussed in this article.

Taking into account the accepted conditions, it is shown that for a single irregularity of type 1, derailment of wheels is possible with values of a=95-100 mm, L=6 m, and for a double-sided irregularity of type 2 with a=80 mm, L =6 m.

An analysis of the oscillograms of the total longitudinal forces between adjacent units of the rolling stock, depending

on the distance traveled, showed that, due to the presence of buffer devices, braking is shockless, except for the connection between the locomotive and the first wagon.

The estimated braking distance was 583 m from the moment the sudden braking was applied, it should be noted that this value is within the limits of current standards and complies with regulatory and technical documents.

As studies have shown, the derailment of wagons is not possible in the case of a shift of the rail-sleeper lattice caused by an increase in the magnitude of the transverse forces acting from the side of the wheels on the rails during braking. This is due to the fact that the frame forces obtained in the simulation have little effect on the track in the coastdown mode and, as a rule, have higher values in practice.

The developed modeling framework establishes a solid foundation for future expansion into AI-assisted digital twins of railway dynamics. Incorporating environmental effects, adaptive friction modeling, and field-sensor data will enhance its reliability for predictive maintenance, safety assessment, and automated control applications in next-generation intelligent railway systems.

A limitation of the present model is the absence of an explicit thermal–mechanical coupling. Although temperature-induced irregularities were geometrically implemented, the model does not simulate the redistribution of thermal stresses or the progressive rail expansion that occurs in continuous welded track under seasonal temperature variation. This limits the ability to assess temperature-driven buckling, rail creep, and time-dependent deformation phenomena that can affect dynamic stability. Incorporating the temperature variable as a continuous parameter influencing the rail stiffness matrix and sleeper–ballast interaction would significantly improve the physical realism of future simulations.

Chain-effect verification. Earlier drafts assessed derailment risk on single-wagon models. In the revised model, derailment is treated as an event that changes the contact and resistance states of the initiating wagon, and the resulting longitudinal force waves are traced through the full consist in UM. The results (Figs. S33-S35 and Figs.10–12, KPIs in Table S3) show that (i) forces concentrate first at the wagon 9 interface, (ii) attenuation prevents formation-wide shocks in Options 1–2, and (iii) in Option 3 a tensile wave reaches the locomotive ∼150 m downstream of the initiating event without exceeding design limits. Thus, the impact of one wagon's derailment on front and rear vehicles is explicitly quantified and aligns with our earlier qualitative interpretation.[41]

Acknowledgments

This work has been supported financially by the research project (BR 27195331 - To develop a multifunctional robotic system for military use with the ability to search for and neutralize mines, ammunition and improvised devices) of the Ministry of Education and Science of the Republic of Kazakhstan and was performed at Research Institute of Communications and Aerospace Engineering in Almaty University of Power Engineering and Telecommunications named after G. Daukeyev, which is gratefully acknowledged by the authors.

Conflict of Interest

The authors confirm that they have no conflict of interest with respect to the work described in this manuscript.

Supporting Information

Applicable.

CRediT Statement

Janat Musayev: Investigation, Writing - Original draft preparation, Visualization, Project administration. **Algazy Zhauyt:** Conceptualization, Methodology, Software, Writing - Original draft preparation, Supervision, Project administration. **Vladimir Solonenko:** Validation, Writing - Original draft preparation, Funding acquisition. **Kuanysh Alipbayev:** Resources, Writing - Review and editing, Funding acquisition. **Gulbarshyn Smailova:** Resources, Formal analysis, Writing - Original draft preparation, Project administration. **Nazgul Kaliyeva:** Resources, Writing - Review and editing, Funding acquisition. **Nurgul Kurmangaliyeva:** Resources, Formal analysis, Writing - Original draft preparation, Project administration.

References

[1] J. Musayev, Zh. Abilkaiyr, T. Kaiym, A. Alpeisov, A. Alimbetov, A. Zhauyt, The interaction of the freight car and way taking into account deformation of assembled rails and sleepers, *Vibroengineering Procedia*, 2016, **8**, 269-274.

[2] V. Solonenko, N. Mahmetova, J. Musayev, M. Kuashnin, A. Zhauyt, T. Buzauova, Modeling of dynamic characteristics of freight car withoptimized parameters of wedge-type shock absorber, *Journal of Vibroengineering*, 2017, **19**, 1197-1213, doi: 10.21595/jve.2017.16901.

[3] M. Günay, M. E. Korkmaz, R. Özmen, An investigation on braking systems used in railway vehicles, *Engineering Science and Technology, an International Journal*, 2020, **23**, 421-431, doi: 10.1016/j.jestch.2020.01.009.

[4] T. Zhu, S. Xiao, C. Lei, X. Wang, J. Zhang, B. Yang, G. Yang, Y. Li, Rail vehicle crashworthiness based on collision energy management: an overview, *International Journal of Rail Transportation*, 2021, **9**, 101-131, doi: 10.1080/23248378.2020.1777908.

[5] P. Liu, K. Wang, D. Zhang, Influence of traction and braking operation on wheel-rail dynamic interaction for heavy haul locomotive, *China Railway Science*, 2017, **38**, 96-104, doi: 10.3969/j.issn.1001-4632.2017.02.15.

[6] J. Ali Zakeri, H. Xia, Sensitivity analysis of track parameters on train-track dynamic interaction, *Journal of Mechanical Science and Technology*, 2008, **22**, 1299-1304, doi: 10.1007/s12206-008-0316-x.

[7] A. V. Vostroukhov, A. V. Metrikine, Periodically supported

beam on a visco-elastic layer as a model for dynamic analysis of a high-speed railway track, *International Journal of Solids and Structures*, 2003, **40**, 5723–5752, doi: 10.1016/S0020-7683(03)00311-1.

[8] J. A. Zakeri, Computer simulation for dynamics of railway track structures, Ph. D. Thesis, Northern Jiaotong University, 2000.

[9] J. A. Zakeri, H. Xia, J. J. Fan, Effects of unsupported sleeper on dynamic responses of railway track, *Journal of Beijing Jiaotong University*, 2000, **24**, 1, 50–55.

[10] T. Gao, J. Cong, P. Wang, J. Liu, Y. Wang, Q. He, Vertical track irregularity analysis of high-speed railways on simply-supported beam bridges based on the virtual track inspection method, *Proceedings of the Institution of Mechanical Engineers, Part F: Journal of Rail and Rapid Transit*, 2021, **235**, 328-338, doi: 10.1177/0954409720924574.

[11] H. Li, W.-G. Yang, P. Liu, M. Wang, Prediction method and experimental verification of vibration response caused by underground high-speed railways, *Journal of Low Frequency Noise, Vibration and Active Control*, 2023, **42**, 452-469, doi: 10.1177/14613484221132117.

[12] B. Olivier, O. Verlinden, G. Kouroussis, Comparison of X‐T and X‐X co-simulation techniques applied on railway dynamics, *Multibody System Dynamics*, 2022, **55**, 39-56, doi: 10.1007/s11044-022-09821-4.

[13] I. Bondarenko, R. Keršys, L. Neduzha, Analysis of problem related to experimental data processing in the study of the rolling stock influence on the track, *In Proceedings of the 26th International Conference Transport Means*, Kaunas, Lithuania, 5–7 October 2022, 663–668.

[14] H. Doi, T. Hondo, Y. Nishiyama, S. Kuniyuki, T. Tanaka, Stationary test method for evaluating wheel unloading of railway vehicle on twisted track simulated with spacers between wheel and rail, *The Proceedings of the Transportation and Logistics Conference*, 2020, **29**, 3801, doi: 10.1299/jsmetld.2020.29.3801.

[15] H. Wang, J. Berkers, N. van den Hurk, N. F. Layegh, Study of loaded versus unloaded measurements in railway track inspection, *Measurement*, 2021, **169**, 108556, doi: 10.1016/j.measurement.2020.108556.

[16] E. F. de Souza, T. N. Bittencourt, D. Ribeiro, H. Carvalho, Feasibility of applying mel-frequency cepstral coefficients in a drive-by damage detection methodology for high-speed railway bridges, *Sustainability*, 2022, **14**, 13290, doi: 10.3390/su142013290.

[17] DSTU 7571:2014; Railway rolling stock permissible exposure norms to the railway track width 1520 mm, Minekonomrozvitku, Kyiv, Ukraine, 2015.

[18] M. A. Spiroiu, M. Nicolescu, On the estimation of the reliability probabilistic model of railway wheelset, *IOP Conference Series: Materials Science and Engineering*, 2019, **682**, 012001, doi: 10.1088/1757-899x/682/1/012001.

[19] K. Wang, C. Huang, W. Zhai, P. Liu, S. Wang, Progress on wheel-rail dynamic performance of railway curve negotiation, *Journal of Traffic and Transportation Engineering (English Edition)*, 2014, **1**, 209-220, doi: 10.1016/S2095-7564(15)30104-5.

[20] K. W. Ahmed, S. Sankar, Steady-state curving performance of railway freight truck with damper-coupled wheelsets, *Vehicle System Dynamics*, 1988, **17**, 295-315, doi: 10.1080/00423118808968908.

[21] Y. M. Cherkashin, D. Y. Pogorelov, V. A. Simonov, Influence of rolling stock and track parameters on train traffic safety, *Vestnik VNIIZhT*, 2010, **2**, 11-20, doi: 10.20295/2223-9987-2024-04-96-102.

[22] C. Mao, Study on curving performance for bogie with magnetic fluid coupled wheelsets, *Journal of the China Railway Society*, 2002, **24**, 28-33.

[23] R. V. Dukkipati, S. Narayana Swamy, Lateral stability and steady state curving performance of unconventional rail trucks, *Mechanism and Machine Theory*, 2001, **36**, 577-587, doi: 10.1016/S0094-114X(01)00006-4.

[24] E. Di Gialleonardo, F. Braghin, S. Bruni, The influence of track modelling options on the simulation of rail vehicle dynamics, *Journal of Sound and Vibration*, 2012, **331**, 4246-4258, doi: 10.1016/j.jsv.2012.04.024.

[25] Y. H. Huang, F. Li, M. H. Fu, Research on curving performance of a bogie with independently rotating wheels, *China Railway Science*, 2001, **22**, 6, 7-11.

[26] B. Kurzeck, Combined friction induced oscillations of wheelset and track during the curving of metros and their influence on corrugation, *Wear*, 2011, **271**, 299-310, doi: 10.1016/j.wear.2010.10.049.

[27] S. Y. Lee, Y. C. Cheng, Influences of the vertical and the roll motions of frames on the hunting stability of trucks moving on curved tracks, *Journal of Sound and Vibration*, 2006, **294**, 441-453, doi: 10.1016/j.jsv.2005.10.025.

[28] Z. G. Lu, H. X. Zhao, Curve performance study and parameter design of flexible coupled single-wheelset running gears, *China Railway Science*, 2004, **25**, 32-37.

[29] P. T. Ni, K.W. Wang, J. Chen, et al. Influence of anti-hunting damper on critical velocity and high-speed curve negotiating performance of the vehicle with MRF coupled wheelsets, *Journal of the China Railway Society*, 2007, **29**, 34-39.

[30] Z.S. Ren, S.G. Sun, Study on the influence of parameters to the dynamics of light rail vehicles with independently rotating wheel, *Electric Locomotive and Mass Transit Vehicles*, 2003, **26**, 22-24.

[31] I. Bondarenko, V. Lukošević̆ius, R. Keršys, L. Neduzha, Investigation of dynamic processes of rolling stock‐track interaction: experimental realization, *Sustainability*, 2023, **15**, 5356, doi: 10.3390/su15065356.

[32] Q. Wang, D. Li, J. Zeng, X. Peng, L. Wei, W. Du, A diagnostic method of freight wagons hunting performance based on wayside hunting detection system, *Measurement*, 2024, **227**, 114274, doi: 10.1016/j.measurement.2024.114274.

[33] S. K. Sharma, Multibody analysis of longitudinal train dynamics on the passenger ride performance due to brake application, *Proceedings of the Institution of Mechanical*

Engineers, *Part K*: *Journal of Multi-body Dynamics*, 2019, **233**, 266-279, doi: 10.1177/1464419318788775.
[34]https://www.universalmechanism.com/en/plugins/catalogue/index.php id=3&utm_source=chatgpt.com.
[35] L. Cantone, D. Negretti, V. Vullo, Evaluation of the admissible longitudinal compressive forces by means of multibody train simulations, *In Proceedings of the First International Conference on Railway Technology: Research, Development and Maintenance, J. Pombo, (Editor)*, Civil-Comp Press, Stirlingshire, Scotland. J. Pombo, Tor Vergata University of Rome, Italy, 18 April 2012, doi: 10.4203/ccp.98.26.
[36] N. Bosso, M. Magelli, N. Zampieri, A numerical method for the simulation of freight train emergency braking operations based on the UIC braked weight percentage, *Railway Engineering Science*, 2023, **31**, 162-171, doi: 10.1007/s40534-022-00296-9.
[37] V. V. Krishna, D. Jobstfinke, S. Melzi, M. Berg, An integrated numerical framework to investigate the running safety of overlong freight trains, *Proceedings of the Institution of Mechanical Engineers*, *Part F*: *Journal of Rail and Rapid Transit*, 2021, **235**, 47-60, doi: 10.1177/0954409720905203.
[38] N. Burgelman, Z. Li, R. Dollevoet, Fast estimation of the derailment risk of a braking train in curves and turnouts, *International Journal of Heavy Vehicle Systems*, 2016, **23**, 213, doi: 10.1504/ijhvs.2016.077320.
[39] H. Zhao, P. Xu, B. Li, S. Yao, C. Yang, W. Guo, X. Xiao, Full-scale train-to-train impact test and multi-body dynamic simulation analysis, *Machines*, 2021, **9**, 297, doi: 10.3390/machines9110297.
[40] W.M. Zhai, Z. L. Han, Z. W. Chen, L. Ling, S.Y. Zhu, Train track bridge dynamic interaction: a state-of-the-art review, *International Journal of Vehicle Mechanics and Mobility*, 2019, **57**, 984-1027, doi: 10.1080/00423114.2019.1605085.

Publisher's Note: Engineered Science Publisher remains neutral with regard to jurisdictional claims in published maps and institutional affiliations.

Open Access
This article is licensed under a Creative Commons Attribution-NonCommercial-NoDerivatives 4.0 International, which permits the use, sharing, adaptation, distribution and reproduction in any medium or format, as long as appropriate credit to the original author(s) and the source is given by providing a link to the Creative Commons license. This usage for commercial purposes is not allowed. If modifications, adaptations or any other transformation were made, it is not allowed for distribution. The images or other third-party material in this article are included in the article's Creative Commons license, unless indicated otherwise in a credit line to the material. If material is not included in the article's Creative Commons license and your intended use is not permitted by statutory regulation or exceeds the permitted use, you will need to obtain permission directly from the copyright holder. To view a copy of this license, visit https://creativecommons.org/licenses/by-nc-nd/4.0/.

©The Author(s) 2026.